Cryo-electron tomography reveals the structural diversity of cardiac proteins in their cellular context

Rahel A. Woldeyes[1], Masataka Nishiga[2,3], Alison S. Vander Roest[4,5], Leeya Engel[6,7], Prerna Giri[2,4], Gabrielle C. Montenegro[1], Andrew C. Wu[1], Alexander R. Dunn[7], James A. Spudich[8], Daniel Bernstein[2,4], Michael F. Schmid[1,9], Joseph C. Wu[2,3] and Wah Chiu[1,9 *]

[1]Department of Bioengineering, Stanford University, Stanford, CA, USA
[2]Stanford Cardiovascular Institute, Stanford University School of Medicine, Stanford, CA, USA
[3]Division of Cardiovascular Medicine, Stanford University School of Medicine, Stanford, CA, USA
[4]Department of Pediatrics, Stanford University School of Medicine, Stanford, CA, USA
[5]Department of Biomedical Engineering, University of Michigan, MI, USA
[6]Faculty of Mechanical Engineering, Technion - Israel Institute of Technology, Haifa, Israel
[7]Department of Chemical Engineering, Stanford University, Stanford, CA, USA
[8]Department of Biochemistry, Stanford University School of Medicine, Stanford, CA, USA
[9]Division of Cryo-EM and Bioimaging, SSRL, SLAC National Accelerator Laboratory, Stanford University, Menlo Park, CA, USA

*To whom the correspondence should be addressed: wahc@stanford.edu

Abstract

Cardiovascular diseases are a leading cause of death worldwide, but our understanding of the underlying mechanisms is limited, in part because of the complexity of the cellular machinery that controls the heart muscle contraction cycle. Cryogenic electron tomography (cryo-ET) provides a way to visualize diverse cellular machinery while preserving contextual information like subcellular localization and transient complex formation, but this approach has not been widely applied to the study of heart muscle cells (cardiomyocytes). Here, we deploy a platform for studying cardiovascular disease by combining cryo-ET with human induced pluripotent stem cell–derived cardiomyocytes (hiPSC-CMs). After developing a cryo-ET workflow for visualizing macromolecules in hiPSC-CMs, we reconstructed sub-nanometer resolution structures of the human thin filament, a central component of the contractile machinery. We also visualized a previously unobserved organization of a regulatory complex that connects muscle contraction to calcium signaling (the troponin complex), highlighting the value of our approach for interrogating the structures of cardiac proteins in their cellular context.

Introduction

Advances in the field of cryogenic electron tomography (cryo-ET) are making it feasible to study macromolecular structure and function in the native environment of cells at high enough resolution to dissect mechanism[1]. This technology has the potential to revolutionize our approach to structural biology, but technical challenges have historically slowed its widespread adoption. For example, difficulties with sample preparation have focused early seminal work on cells that are thin enough to be transparent under transmission electron microscopes[2], but advances like cryo–focused ion beam (cryo-FIB) milling now enable the examination of thicker cell types[3–5]. Recognizing the potential of the technology to study the complex biology of heart muscle cells (cardiomyocytes), we set out to develop a cryo-ET platform for studying cardiovascular structural biology.

There is an outstanding need for new approaches in cardiobiology. Heart disease is one of the leading causes of death worldwide, and our ability to treat and prevent it is hampered by a lack of mechanistic understanding of the many different causes that lead to heart failure and death. Mutations associated with cardiomyopathy occur in many of the proteins that constitute the regulatory system that controls heart muscle contraction, but the effect of these mutations on the structure and function of cardiac proteins remains unclear. Drug-induced cardiotoxicity is a troubling side effect for many patients undergoing various cancer treatments, but the mechanisms of cardiotoxicity of different drugs are unclear. With detailed structural information on the structural consequences of cardiomyopathy-associated mutations or the direct mechanisms of drug-induced cardiotoxicity, we could accelerate the design of treatments to combat these diseases. However, the number of components and the complexity of their interactions during normal cardiomyocyte function has been a challenge for building predictive models of the impact of these perturbations on the function of the larger system.

Cardiomyocytes (CMs) have a complex regulatory system that controls our regular heartbeat. Multiple cellular compartments coordinate to regulate the release of calcium into the cytoplasm, which binds to myofibrils to initiate contraction. Myofibrils are macromolecular complexes that directly generate the force of contraction. They are composed of thin and thick filaments interwoven into muscle fibers, with the repeating unit of organization known as the sarcomere. The thick filaments are mostly made up of the protein myosin. The thin filaments are made up of the actin filament, tropomyosin, which lays across actin, and the troponin complex, which binds both actin and tropomyosin and mediates the initiation of contraction by calcium. When calcium binds to the troponin complex, it induces a conformational shift of tropomyosin that exposes myosin binding sites on the thin filament. Upon binding, the myosin head mediates a shift in the relative position of the thick and thin filaments to generate the force required for contraction. Myofibrils in human cardiomyocytes are further made up of many interaction partners and distinct proteins not mentioned above that contribute to their proper organization and structure.

A cryo-ET centered approach has the potential to tackle the complexity of cardiovascular structural biology by directly imaging macromolecular components as they are assembled in cells. Indirect effects of drug-induced cardiotoxicity, like those that depend on active mitochondrial metabolism, can be studied by using living cells as an experimental system. The impact of cardiomyopathy-associated mutations on protein structure can be studied in a physiologically relevant context by avoiding isolation protocols. Initial efforts towards this goal have already been illuminating. Cryo-ET imaging of myofibrils isolated from mouse cardiomyocytes provided insight into the interactions between myosin and actin that drive muscle contraction[6,7]. Imaging of neonatal rat cardiomyocytes with cryo-ET revealed the

structure and organization of thin filaments[8]. However, important questions remain about the structure of the myofibril in human cells.

To answer these questions and advance the technology, we developed a complementary cryo-ET workflow for studying cardiovascular biology. First, we used human induced pluripotent stem cell–derived cardiomyocytes (hiPSC-CMs) as a model system for cardiac structural biology. hiPSC-CMs are advantageous because human primary-CMs cannot be maintained in culture for functional studies. There are also key differences between human and rodent CMs that limit the applicability of rodent cells for studying human disease. Additional advantages of hiPSC-CMs include a pre-existing availability of hiPSC-CMs derived from several genetic backgrounds, CRISPR-based tools to perform genome editing and introduce disease-relevant mutations in isogenic backgrounds, and cell lines with fluorescently tagged proteins useful for the study of cardiovascular biology. Second, we developed a workflow using cryo-ET that incorporates several advances, including micropatterning of electron microscopy grids, correlated cryogenic light and focused ion beam microscopy, cryogenic electron tomography and cutting-edge approaches in data processing.

To demonstrate the utility of our workflow, we reconstructed structures of the thin filament from hiPSC-CMs that included the regulatory proteins of the troponin complex and tropomyosin. We then used the platform to study the impact of two disease-relevant perturbations on thin filament structure: a mutation associated with hypertrophic cardiomyopathy ($MYH7^{WT/G256E}$) that leads to hypercontractility[9], and treatment with doxorubicin, an anti-cancer agent with cardiotoxic side effects that include disruption of the myofibril superstructure[10]. We found impacts on thin filament structure by these perturbations that likely reflect a response to changes in the local environment of the myofibril, highlighting the potential of our approach for dissecting physiologically relevant structural biology in human cardiomyocytes.

Results

Optimized experimental cryo-ET workflow for the visualization of macromolecules in cardiomyocytes

We started this study by optimizing a cryogenic electron tomography (cryo-ET)–based experimental workflow (**Fig. 1**, **Fig. S1**) to visualize macromolecules in cardiomyocytes at sub-nanometer resolution. We incorporated several advances into the workflow to overcome technical challenges associated with cardiomyocytes and achieve sub-nanometer resolution reconstructions.

In the first step of the workflow, we differentiated human induced pluripotent stem cells into cardiomyocytes (hiPSC-CMs) using an established protocol (**Methods**), then bound them to micropatterned electron microscopy (EM) grids. We used micropatterned EM grids to avoid overcrowding of cells, center cells on EM grid squares, and provide spatial cues to improve the organization of contractile proteins within the cells. The pattern consisted of rectangles with a length to width ratio of 7:1, designed to mimic the dimensions of human adult cardiomyocytes and shown to optimize contractile function[11] (**Fig. S1b**). Depending on the experiment, the hiPSC-CMs contained a genetically encoded fluorescent tag for alpha-actinin, a component of the myofibril structure that generates the contractile force driving heart beats. This fluorescent tag allowed us to easily evaluate the performance of our micropatterned EM grids. Indeed, we found that they eliminated overcrowding, centered cells on the grid squares (**Fig. 1a**), and increased the organization of contractile proteins within the cells (**Fig. 1b**).

After binding hiPSC-CMs to the EM grids, we used cryo-focused ion beam (cryo-FIB) milling to prepare approximately 150 nm thick lamellae for cryogenic electron tomography (cryo-ET). When possible, we used the fluorescent signal from tagged alpha-actinin to select only hiPSC-CMs with high intracellular organization for cryo-FIB milling and imaging. Integrating in-chamber fluorescent microscopes into the cryo-FIB/SEM was an important instrumentation advance that simplified the workflow and increased throughput.

Lamellae from the hiPSC-CMs revealed the characteristic ultrastructures of a cardiomyocyte, even at a lower magnification (**Fig. 1c**). We detected mitochondria of various shapes and sizes, regions of sarcoplasmic reticulum (SR), and myofibrils that were subdivided into individual sarcomeres at clearly demarcated Z-lines (**Fig. 1c**). Each of the ultrastructures mentioned play a critical role for cardiomyocytes in maintaining a regular heartbeat.

We focused on the myofibrils in this work. We collected high-magnification tilt-series images of these regions and reconstructed 3D volumes to better visualize myofibril proteins in their cellular context (**Fig. 2**). We identified the major components of the myofibril from Z-slices of the 3D volume, including both the thick and thin filaments (**Fig. 2a-c**). 3D segmentation of the tomograms, allowed us to better visualize how these filaments are found intertwined in the A-band regions of the sarcomere (**Fig. 2d-e**) (**Movie S1 & S2**). In the I-band, the thin filaments extend toward the Z-lines (**Fig. 2d-e**). Myosin heads can be detected protruding from the thick filaments, with some bridging to the thin filaments (**Movie S1**). Many of the tomograms capture other macromolecules in the immediate vicinity of the myofibril, including ribosomes, glycogen, vesicles, and mitochondria.

Cryo-ET reveals *in situ* structures of the human cardiac thin filament

To demonstrate the utility of our platform for determining sub-nanometer resolution structures of cardiac macromolecules, we sought to reconstruct the human cardiac thin filament using sub-volume averaging of the tomograms (**Fig. S2**, **Table S1**). We trained a convolutional neural network (CNN) to annotate the thin and thick filaments, as well as the membrane and ribosomes in our tomograms. We used the coordinates for the thin filament in wild type hiPSC-CMs to obtain an 8.7 Å global resolution reconstruction of the wild-type thin filament (**Fig. 3b**). The main components of the thin filaments, filamentous actin and tropomyosin, are clearly resolved (**Fig. 3c**). In the core of the filament, the resolution ranged from 6–8.5 Å. In areas with tropomyosin the resolution ranged from 8–10.5 Å, suggesting more flexibility in the position of tropomyosin compared to the actin filament. The helices in individual actin monomers are visible, as expected for the resolution of the map, and individual coiled-coil models of tropomyosin (PDB-6KN8) can be fitted into the density map.

The current model of the cardiac contraction cycle[12,13] posits that tropomyosin shifts relative to actin in response to calcium binding to expose myosin binding sites on the actin. Three conformational states of tropomyosin have been described as part of the contraction cycle: the calcium-free B-state, the calcium-bound C-state, and the myosin-bound M-state[14]. To determine the functional state of our *in situ* map, we compared it to previously determined maps of the B-state (EMD-0728), C-state (EMD-0729), and M-state (EMD-13996). Interestingly, the position of tropomyosin relative to actin in our map is in between the C- and M-state (**Fig. 3d**). This suggests that our map represents a state of the thin filament that is poised for myosin binding.

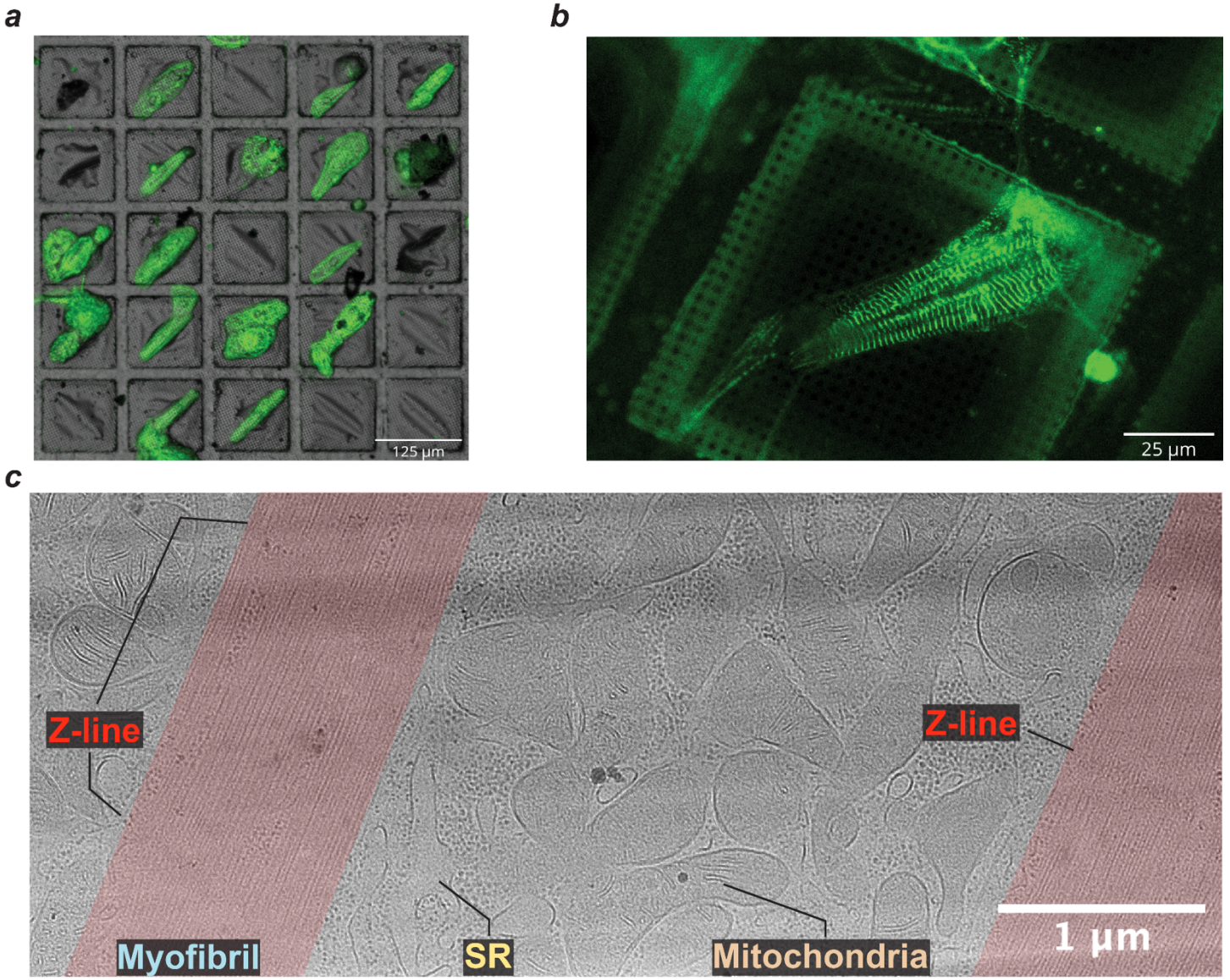

Figure 1 | An experimental workflow for visualization of hiPSC-derived cardiomyocytes ultrastructure using cryo-electron tomography.

a Light microscopy overview of human induced pluripotent stem cell–derived cardiomyocytes (hiPSC-CMs) expressing fluorescently tagged α-actinin. Cells are attached to a micropatterned grid to guide hiPSC-CM attachment and shape.

b High magnification fluorescent imaging within the FIB-SEM is used to guide the lamella generation.

c Cryo-TEM image collected on a lamella highlighting region with the myofibrils (highlighted in red), the sarcoplasmic reticulum (SR), and mitochondria.

To determine the effect of mutations on thin filament structure, we used the workflow to image and reconstruct thin filaments from mutant hiPSC-CMs carrying the $MYH7^{WT/G256E}$ allele. This mutant allele has been shown to have a hypercontractility phenotype, possibly through increased availability of the mutant myosin heads to bind the thin filament[9]. The thin filament was reconstructed from the $MYH7^{WT/G256E}$ background to an 9.3 Å resolution (Fig. S3a). We can clearly see the resolved helices in the actin filament, and the tropomyosin is resolved well enough for comparison to the wild-type. The two maps overlay well, with a RMSD of 2.7 Å between the models fitted into these maps (Fig. 3e). The agreement between these maps supports a model in which full movement of tropomyosin to the M-state requires myosin binding.

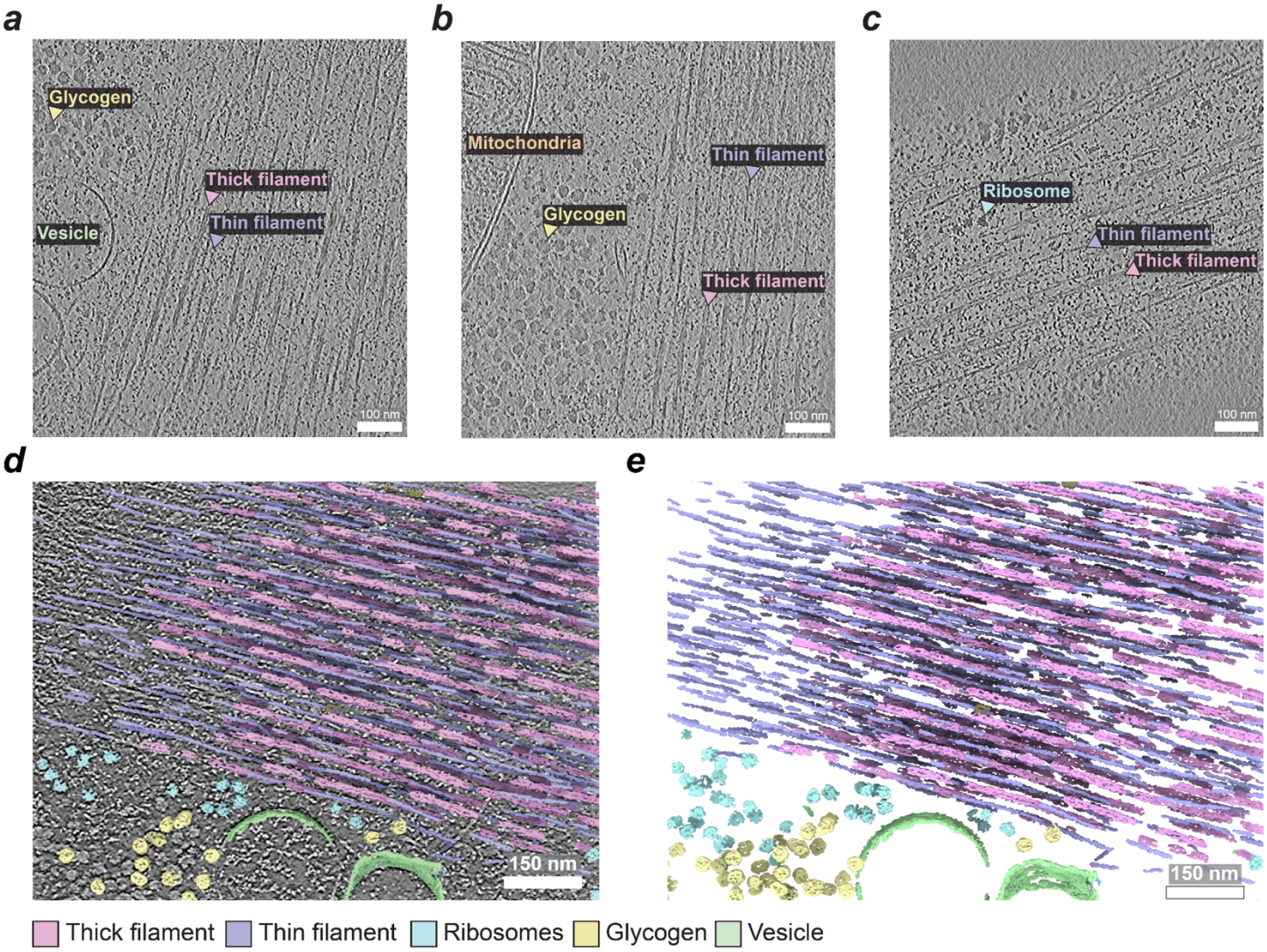

Fig. 2 | Subcellular arrangement of macromolecules in cardiomyocytes

a,b,c Cryo-ET images collected on a hiPSC-CM lamella, highlighting different regions with vesicles (green), glycogen (yellow), ribosomes (teal), mitochondria (orange), and the thick (pink) and thin (purple) filaments of myofibrils.

d Segmentation of the tomogram found in ***a*** (rotated by 90° anticlockwise) highlights the variety of macromolecules present, including part of a myofibril with thick (pink) and thin (purple) filaments, vesicles (green), glycogen (yellow) and ribosomes (teal) within the field of view.

e Segmented features from ***d*** are shown without the tomogram slice in the background.

We next used doxorubicin treatment as an alternative approach for perturbing thin filament structure by treating hiPSC-CMs with 100 nM doxorubicin for 24 hours before processing and imaging them. Doxorubicin is an anti-cancer drug with a known side-effect of cardiac toxicity. Doxorubicin-induced cardiac toxicity has been associated with sarcomeric disarray and deterioration of myofibrils[10,15]. The mechanisms driving myofibrillar deterioration are primarily due to oxidative injury, especially to the mitochondria, and the effects on the sarcomere are likely indirect. Given our still incomplete understanding of the full nature of doxorubicin-induced cardiac toxicity, our platform provided a unique opportunity to determine the structural effects of doxorubicin on sarcomeric structure at high resolution. We started by reconstructing the thin filament map to 9.5 Å resolution from doxorubicin-treated wild type hiPSC-CMs (Fig. S3c). We found a significant shift in tropomyosin positioning towards the C-state and away from the M-state (Fig. S3d). We were interested to note that, even in a drug-treated state

associated with visible sarcomeric disarray, tropomyosin adopted a conformation that was similar to the C-state in hiPSC-CMs (Fig. 3f). This suggests that a conformation similar to the calcium-bound state is the resting state for tropomyosin in hiPSC-CMs. The difference between the drug-treated (C-like) and drug-free (intermediate) tropomyosin conformations also suggest that an altered sarcomeric environment contributes to the tropomyosin conformation found in hiPSC-CMs.

The troponin complex adopts a variety of conformations in the cellular context

Reconstructing the structure of thin filaments in hiPSC-CMs gave us an opportunity to explore their local neighborhoods within the tomograms, identify additional binding partners, and expand our model of the sarcomeric proteins. Using the thin filament reconstructions, we focused on regions at the filament crosspoints where the troponin complexes are located. Classifying and refining these regions of interest, we reconstructed the structure of the troponin complex bound to the thin filament. The troponin complex, a key regulator of muscle contraction, is composed of the calcium binding subunit troponin C (cTnC), the regulatory subunit troponin I (cTnI), and the tropomyosin binding subunit troponin T (cTnT) (Fig. S4). The troponin complex is known to assemble at two adjacent sites on the thin filament (the upper and lower complexes) (Fig. 4b) and, in response to calcium binding at cTnC, the troponin complex shifts the position of tropomyosin to uncover myosin binding sites and initiate contraction[16]. Recent studies using reconstituted or isolated thin filaments have shown that the upper and lower troponin complexes can adopt a combination of calcium-free and calcium-bound conformations at various calcium levels[17,18]. However, the native structure of the troponin complex in cardiac cells is unknown. Our reconstructions of the troponin complexes bound to the thin filament had a resolution of 19.5 Å for wild type, and a resolution of 12.4 Å for both the mutant and doxorubicin-treated cells (Table S1).

Given the unique position of tropomyosin in the thin filaments reconstructed from hiPSC-CMs (Fig. 3c,d), and the central role of the troponin complex in controlling tropomyosin positioning, we were interested in comparing the conformations of tropomyosin and the troponin complex under the same three conditions. Consistent with our reconstructions of the thin filament alone, we found tropomyosin in an intermediate conformation between C-state and M-state, with a shift towards the C-state in doxorubicin treated cells. In wild-type hiPSC-CMs, a model of the two troponin complexes in a calcium-bound state (PDB:6KN8) fit best (Fig. 4b,c). Using this model as a reference, we observed weak density at the position of cTnC (Fig. 4c**, exposed blue model**) and the switch helix of cTnI (Fig. 4c**, exposed pink model,** Fig. S4) in the *in situ* maps of both complexes. The maps of the upper and lower complexes also diverged at the locations of cTnC and the cTnT-cTnI coiled-coil (Fig. 4c, Fig. S4, Movie S3&S4)**.**These conformations of the troponin complex have not been observed in previous studies, and may reflect an interaction between the troponin complex and additional factors in the sarcomere that bind the thin filament, like myosin heads and myosin binding protein C.

In hiPSC-CMs carrying the MYH7$^{WT/G256E}$ mutation, the differences between the upper and lower complexes were more pronounced (Fig. 4d). The model of the troponin complex in a calcium bound state fits well within the lower complex, but density for the upper complex as a whole was significantly weaker at the same map contour level (Fig. 4d **top,** Movie S3&S4). This asymmetry between sites may reflect an increase in cross-bridge interactions due to the mutant background.

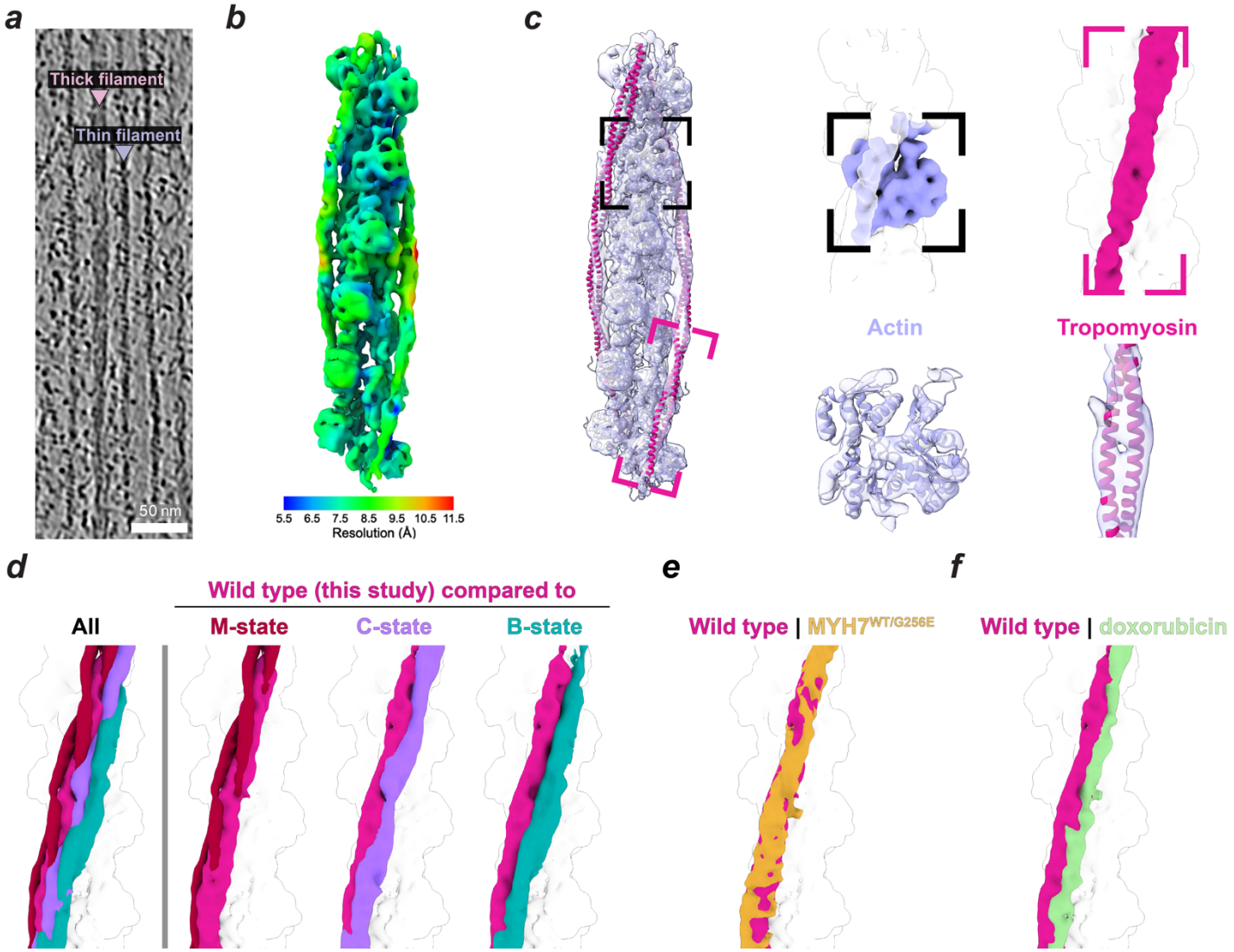

Fig. 3 | *In situ* structures of the human thin filament.

a An example tomogram slice showing both thick (pink) and thin (purple) filaments.

b The structure of the repeating unit of the thin filament, reconstructed from hiPSC-CMs. Actin and tropomyosin subunits are both visible. The resolution of the reconstruction is represented as a colormap.

c A molecular model of the thin filament was fit within the *in-situ* reconstruction. (Far left) A full molecular mode of the thin filament repeating unit is shown, including filamentous actin (purple) and tropomyosin (hot pink). (Top left) The position of a single actin subunit (purple) is highlighted within the larger reconstruction (transparent white). (Bottom left) A molecular model of actin (PDB: 6KN8) fits within the *in situ* map. Individual helices can be resolved within the actin subunit. (Top right) Tropomyosin (hot pink) is highlighted within the larger reconstruction (transparent white). (Bottom right) A molecular model of tropomyosin (PDB: 6KN8) fits within the *in situ* map.

d The position of tropomyosin in the *in situ* structure is in between the M-state and C-state. (All) The position of tropomyosin is shown in relation to the M-state (burgundy) C-state (purple) and B-state (teal). (M-state) The position of tropomyosin with respect to the M-state (EMD-13996), associated with myosin binding to the thin filament. (C-state) The structure of tropomyosin with respect to the C-state (EMD-0729), a calcium-bound conformation of the thin filament without myosin binding. (B-state) The position of tropomyosin with respect to the B-state (EMD-0728), the apo-state of the thin filament.

e A comparison of tropomyosin positions in structures reconstructed from wild type (hot pink) and $MYH7^{WT/G256E}$ (gold) hiPSC-CMs. The actin subunits are shown as a white outline. The position of tropomyosin in $MYH7^{WT/G256E}$ is similar to that in wild-type hiPSC-CMs.

f Tropomyosin positions in structures reconstructed from wild type (hot pink) and doxorubicin-treated (light green) hiPSC-CMs, depicted as in ***e***. The position of tropomyosin is shifted away from the M-state in doxorubicin-treated cells.

Reconstructing the troponin complex with the thin filament from doxorubicin-treated cells also revealed

pronounced differences from wild type. We fit most of the model of the calcium-bound conformation of the troponin complex into the map, but the map density associated with the cTnT-cTnI coiled-coil was shifted away from the actin in the thin filament (**Fig. 4e, Fig. S4, Movie S3&S4**). The density map is closest to the troponin complex from reconstituted and isolated thin filaments, which could reflect the larger-scale disarray of sarcomeres in response to doxorubicin and a decrease in interactions with binding partners.

Discussion

The regulatory pathways controlling our heartbeat are complex, spanning multiple spatial scales. This has made it difficult to reconstitute the full system using traditional biochemical approaches and hampered our full mechanistic understanding of cardiac pathologies. Here we describe the use of a high resolution cryo-ET platform applied to human induced pluripotent stem cell–derived cardiomyocytes (hiPSC-CMs) to tackle this challenge by directly determining the structure of cardiac proteins in cells. Our platform incorporates multiple advances including micropatterned electron microscopy grids to control hiPSC-CM attachment, correlated cryogenic light and focused ion beam microscopy to prepare representative hiPSC-CMs lamellae for cryo-ET, and cutting-edge advances in data collection and image processing. Using our platform, we've reconstructed six structures of the human cardiac thin filament and measured the response of thin filament structure to both a hypertrophic cardiomyopathy-inducing mutation ($MYH7^{WT/G256E}$) and a cardiotoxic drug (doxorubicin). These efforts demonstrate the utility of our platform for dissecting structural states in the native context of cardiomyocytes and lay the foundation for an exciting new approach to structural cardiobiology.

Our reconstructions of the human thin filament from cardiomyocytes revealed variability in the position of both tropomyosin and the troponin complex on actin in response to different perturbations. We discovered that tropomyosin adopted conformations intermediate to the M-state (myosin bound) and C-state (calcium bound) but no reconstruction resembled the B-state (calcium unbound), even under conditions associated with sarcomeric disarray. This suggests that the B-state may not exist in a stable form in cells or is at least lowly populated. An effective screening approach to identify short-lived states like a fully relaxed cardiomyocyte before calcium-induced calcium release initiates the next contraction will be an important step forward for discovering functionally important conformations of the filament. We also found prevalent asymmetries in the conformation of the two assembly sites of the troponin complex on actin. Expanding our structural understanding of the local environment of thin filaments will be important for understanding the extent that this asymmetry reflects distinct signals, like inter-filament cross bridging.

An immediate and impactful extension of our platform will be to further define protein interactions and post-translational modifications that stabilize the different conformational states of the thin filament. Phenomena of particular interest include phosphorylation of the thin filament through β-adrenergic signaling, which accommodates increased physical activity, as well as reconstructing both the myosin head and myosin binding protein C bound to the thin filament. We also look forward to expanding our study of the precise effects of cardiomyopathy-associated mutations on the structure and function of the thin filament.

Our platform also provides a unique opportunity to determine the conformational states of multiple proteins of the regulatory system controlling contraction, simultaneously, revealing insights into

regulatory mechanisms that would be otherwise difficult to discern. We have observed mitochondria, glycogen, sarcoplasmic reticulum and other macromolecules in close proximity to myofibrils. Strategies to integrate information at the molecular and cellular scales from multiple molecules across multiple compartments will be important for fully realizing the potential of our platform.

We have described a proof of principle that our approach can be used to study the molecular organization of cardiomyocytes, connecting the diverse structures and function of a system of macromolecules as they are coordinated in cells. We expect our platform to catalyze new insights into cardiovascular disease with translational potential. Our work in hiPSC-CMs will also serve as a case study motivating the application of cryo-ET to dissect other complex biological phenomena with impacts on human health.

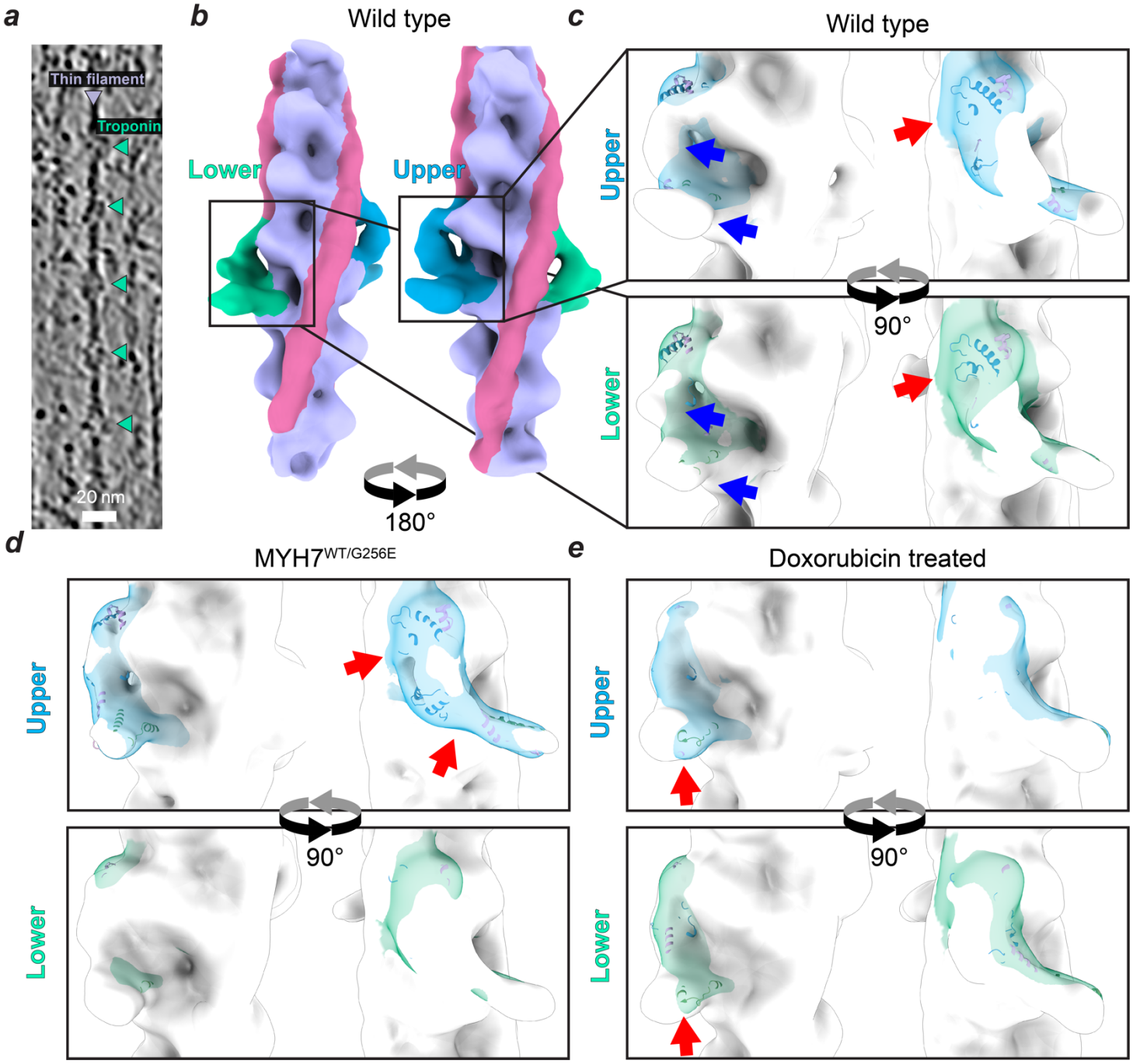

Fig 4 | The *in-situ* structures of the troponin complex reflect distinct local environments of the two sites
a A tomogram slice including a thin filament (purple) with the troponin complexes assembled (green).
b The structure of the thin filament, reconstructed from wild-type cells, with the troponin complex bound. The structure is rotated 180° to highlight the density from troponin at both the lower (green) and upper (blue) sites. The two troponin sites have distinct density maps.
c Differences in density are shown between *in situ* and *in vitro* maps of troponin from wild type hiPSC-CMs. The *in situ* map is shown as an opaque white surface. The *in vitro* map is shown as a transparent surface colored by troponin sites as green (lower), blue (upper), or white (elsewhere). A molecular model of troponin, derived from the *in vitro* map and colored by subunit, is shown as a reference (PDB:6KN8). The troponin subunits shown in the model are C (blue), I (pink), and T (green). Red colored arrows highlight the loss of density *in situ* relative to the *in vitro* map for cTnC and the switch helix of cTnI in both the upper and lower complex. Blue colored arrows highlight the differences *in situ* between the upper and lower sites at cTnC and the cTnT-cTnI coiled-coil.
d The maps are shown for troponin reconstructed from $MYH7^{WT/G256E}$ hiPSC-CMs as in ***c***. Red arrows highlight the relative loss of *in situ* density throughout the troponin complex in the upper site, but not the lower site.
e Troponin complexes reconstructed from doxorubicin-treated hiPSC-CMs are shown as in ***c***. Red arrows highlight the shift of the cTnT-cTnI coiled-coil *in situ* as compared to *in vitro* for both the upper and lower sites.

Methods

Micropatterning of EM grids

Digital files of rectangles with a 1:7 aspect ratio and areas of 2000 μm^2 (16.903 µm by 118.32 µm) and 1500 μm^2 (14.64 µm by 102.465 µm) were generated in *ImageJ*[19] (Digital Files S1 & S2, pixel conversion is 3.58 pixels/µm).

EM grids (UltrAuFoil R2/2 Au 200 mesh Q250AR2A and Quantifoil R2/2 Au 200 mesh Q2100AR2) were micropatterned using the Alveole PRIMO micropatterning system[20–22]. Unpatterned grids were placed holey film up on silicone sheeting (Specialty Manufacturing Inc.) on glass coverslips to prevent them from moving during exposure to plasma and incubation. They were exposed to atmospheric plasma at 22 Watts for 10 seconds using a benchtop plasma etching system (Plasma Etch PE50). The glass coverslip containing the grids was placed on Parafilm (Bemis™ PM999) and several milliliters of 0.01% Poly-L-Lysine (CAS Number 25988-63-0, p4707 Sigma) were added to the surface immediately following the plasma exposure. After 1 hour at room temperature, the grids were rinsed three times in deionized water (DIW) and incubated in a 100 mg/mL solution of mPEG-Succinimidyl Valerate, MW 5,000 (PEG-SVA, Laysan Bio Inc) in 0.1 HEPES (pH 8.5) for 1 hour. They were then rinsed several times in DIW.

Each grid was lifted from the silicone, blotted dry, and held in negative pressure tweezers while 3 µL of a 1:6 solution of photoinitiator (PLPP gel, nanoscaleLABS, LLC) in pure ethanol was added to the surface. Following drying of the PLPP gel, the grids were placed holey-film-down on a glass coverslip and exposed to UV in the Alveole PRIMO photopatterning system at 50 mJ/mm^2. They were then rinsed in DIW several times and stored in 15 µL droplets of DIW contained to custom silicone wells in glass bottom dishes until protein backfill.

hiPSC-cardiomyocyte differentiation and re-plating to EM grids

Wild type and MYH7$^{WT/G256E}$ hiPSC-CMs

The parental WTC hiPSC cell line was generated by the Bruce R. Conklin Laboratory at the Gladstone Institutes and University of California–San Francisco (UCSF)[23]. Cells were maintained as hiPSCs and differentiated into cardiomyocytes using methods described previously[24,25] and available from the Allen Institute for Cell Science webpage (http://allencell.org). AICS-0097-113 ACTN2-mEGFP MYH7$^{WT/WT}$ and AICS-0097-141 ACTN2-mEGFP MYH7$^{WT/G256E}$ were developed via CRISPR/Cas9 gene editing and subjected to quality control at the Allen Institute for Cell Science[9].

hiPSCs were differentiated into cardiomyocytes using an established small-molecule protocol[26] with modifications[25]. Briefly, hiPSCs were seeded onto Matrigel-coated 6-well tissue culture treated plates and maintained for 4 days with mTeSR1 media (85850, Stemcell Technologies). On day 0, hiPSCs were induced with 7.5 μM CHIR99021 (13122, Cayman Chemical) in RPMI 1640 (11875-093, Gibco) and 1X B27 minus insulin (A1895601, Gibco). After 48 hours, the media was replaced with 7.5 μM IWP2 (3533, Tocris) in RPMI 1640 and 1X B27 minus insulin. On day 4, the media was replaced with RPMI 1640 and 1X B27 minus insulin. From day 6 onwards, differentiated cells were maintained in RPMI 1640 and 1X B27 plus insulin (A1895601, Gibco) with media changes every 2-3 days. After the onset of beating (~day 10) cells were grown in RPMI media without glucose with B27 for 4 days and cells were replated on day 15 for subsequent growth and maturation.

On day 48, cells were plated onto the micropatterned electron microscopy grids by lifting with TrypLE and resuspending in replating media (RPMI + B27 with 10% Knock-out Serum Replacement and 10 μM Rock inhibitor) at a density of 100,000 cells/mL. This was done for both control hiPSC-CMs and G256E cells expressing an endogenous fluorescent tag of the sarcomere protein alpha-actinin. The micropatterned grids were held in place in a glass bottom dish with a custom PDMS sticker which enabled the use of small volumes (10-50 μL) of solutions for incubation. After patterning, the grids were sterilized by a 10 min incubation in 70% ethanol, subsequently rinsed in PBS -/- and incubated with a 1:150 dilution of Matrigel in DMEM/F12 media for 1 hour. After removal of the Matrigel solution, 10 μL of replating media were added to each grid, and then approximately 500 cells were added to each grid in 5 μL of resuspension. After 2 hours of attachment, an additional 2 mL of replating media were added to each plate, and then media was replaced with RPMI + B27 after 2 days and cells were cultured for 7-10 days to recover before vitrification.

Doxorubicin treated hiPSC-CMs

Human iPSCs were generated from peripheral blood mononuclear cells collected from healthy donors using Sendai virus and cryopreserved at Stanford CVI iPSC Biobank. Human iPSCs were maintained in Essential 8 (E8) medium (Thermo Fisher Scientific, A1517001) on Matrigel-coated (1:200 dilution, Corning, 356231) 6-well plates. For passaging of hiPSCs, hiPSCs were detached with 0.5mM EDTA and cultured in E8 medium with 10 uM Y-27632 ROCK inhibitor (Selleck Chemicals, S1049) for 24 h. Cardiomyocyte differentiation was carried out in RPMI 1640 (Thermo Fisher Scientific, 11875-119) with B27 supplement minus insulin (Thermo Fisher Scientific, A1895601) when hiPSCs (at passages 20 - 35) reached 80 - 90% confluency, as previously described[10,27,28]. Briefly, hiPSCs were treated with 8 μM CHIR-99021 (Selleck Chemicals, S2924) for 2 days, followed by 1 day recovery, and then 5 uM IWR-1 (Selleck Chemicals, S7086) for another 2 days. Starting from day 7, the differentiation medium

was changed to RPMI 1640 with insulin B-27 Supplement (Thermo Fisher Scientific, 17504044). From day 12, non-cardiomyocytes were removed by glucose starvation using RPMI without glucose (Thermo Fisher Scientific, 11879-020) with B27 supplement for 4 days. The purified cardiomyocytes on day 20-30 were replated using TripLE Select (Thermo Fisher Scientific, A1217701) to cryo-EM grids at the density of 750 cells per grid. To determine the effect of doxorubicin, cardiomyocytes on EM grids were treated with 100 nM of doxorubicin for 24 h. This treatment regimen was chosen to be non-lethal while still impacting hiPSC-CM physiology and gene expression[10].

Vitrification of cardiomyocytes, cryo-CLEM and cryo-FIB milling

Cells were vitrified by plunge freezing into liquid ethane using a Leica EM GP2 plunger. The grids were blotted from the opposite side of the holey film layer at 25 ℃ and 95% humidity.

Cells expressing an endogenous fluorescent tag on alpha-actinin were imaged using the integrated fluorescent light microscope (iFLM) (ThermoFisher Aquilos2 cryoFIB-SEM) to identify cells with ordered sarcomeric arrangement. In early experiments, before the integration of a fluorescent microscope into the FIB chamber of the Aquilos, some grids were visualized using a Zeiss Airyscan2 (LSM800) confocal microscope with Linkam cryostage.

The vitrified cells were then milled to a thickness of ~150 nm using a cryo-FIB, either manually or using the AutoTEM Cryo software (ThermoFisher). The milling was done using a ThermoFisher Aquilos1 or Aquilos2 cryoFIB-SEM with iFLM, following previously described workflows[29,30]. In brief, the grids were sputter coated with metallic platinum using an in-chamber plasma coater to minimize charging. The samples were then coated with a ~500 nm organometallic platinum layer using a gas injection system and additionally sputter coated with a thin layer of platinum. SEM imaging was performed using 2-5 kV and 13 pA current to check milling progress. Milling was performed using a 30 kV ion beam while progressively decreasing the beam current from 300 pA to 30 pA. Micro-expansion joints were used during milling to avoid lamella bending and breakage[31]. Final polishing was performed manually. After polishing, some of the grids were coated with a thin layer of platinum.

Cryo-ET data acquisition, image processing and tomogram reconstruction

Cryo-EM datasets were acquired at 300 kV using Titan Krios transmission electron microscopes (ThermoFisher) equipped with K3 cameras and energy filters (Gatan) (**Table S1**). Data acquisition was performed using SerialEM[32] software. Overview images of the lamellae were collected at 1.04 nm pixel size to identify areas for high-magnification tilt-series data collection. Tilt series projections were acquired at 2.13 Å pixel size (42,000x nominal magnification) using a dose-symmetric[33] data acquisition scheme with 2° or 3° increments starting from 0° or relative to the lamella pretilt. The images were recorded as movies divided into 10 frames. The total dose applied to the sample ranged from 105–120 $e^-/Å^2$. For datasets collected using K3 CDS mode, the targeted dose rate on the camera was 5–6 e^-/pix/s; for non-CDS mode datasets, the targeted dose rate was 10–15 e^-/pix/s.

Individual tilt frames were motion corrected using MotionCor2[34]. The tilt-series were then aligned and reconstructed with dose weighting using AreTomo[35]. The reconstructions were used to select tomograms without crystalline ice, with the correct field of view, and with sufficient contrast. This resulted in a final data set of 12 tomograms (dataset 1), 8 tomograms (dataset 2), and 14 tomograms (dataset 3). For better visualization, CTF-corrected and denoised tomograms were reconstructed using

IsoNet[36] with CTF estimates from Warp[37]. We trained a model that can be used to denoise our full dataset using three representative tomograms. Denoised tomograms were only used for visualization and particle picking, and they were not used in the sub-volume averaging pipeline.

Subvolume averaging

Particle identification

3D convolutional neural network (CNN)–based models were trained to recognize five classes of cellular features: thick filaments, thin filaments, membranes, ribosomes, and background using DeepFinder[38] (**Fig. S2a**, **Movie S1**). Each macromolecule was manually annotated in 4-5 denoised tomograms downsampled by a factor of 4. These coordinates were used to train two CNN models to recognize the different classes. One model was trained on data collected with 2° tilt increments, and the other was trained on data collected with 3° increments. The trained models were used to annotate and pick positions of the thin filament in all of the tomograms. In the first dataset, 92,224 segments of the thin filament were picked from 12 tomograms with an inter-segment distance of 51 Å. In the second dataset, 95,513 segments were picked from 8 tomograms with an inter-segment distance of 68 Å. In the third dataset, 30,249 segments were picked from 14 tomograms with an inter-segment distance of 85 Å.

Thin filament refinement and classification

Sub-volume averaging of the thin filament was performed in RELION 4.0[39] and Warp[37]/M[40]. The motion corrected tilts and tilt-series alignment parameters from AreTomo were imported into Warp, where the tilt-series CTFs were estimated. Pseudo-subtomograms were extracted in RELION using Warp's CTF estimates. Subsets of the data were used for *de novo* initial model generation with C1 symmetry for each of the datasets. The full datasets were then aligned to and refined using the reference and subjected to 3D classification. Selected particles (16,451, 15,147, and 7,555 for dataset 1, 2, and 3, respectively) were further refined in RELION and the results were imported into M. In M, the image-space and volume-space warping grids, the particle poses, and the stage angles were refined in 6 iterations. Starting with iteration 4, CTF parameters were also refined. The final global resolutions were 8.7 Å, 9.3 Å, and 9.5 Å, respectively, for datasets 1–3.

To reconstruct the thin filament with the troponin complex, the subtomograms were recentered towards the cross-point between the 36 nm repeats of the thin filament. After refinement and classification in RELION, the following number of particles were selected for each dataset: 1,463 (dataset 1), 2,114 (dataset 2), and 2,737 (dataset 3). After refinement in M, the final global resolutions for these datasets were 19.5 Å, 12.4 Å, and 12.4 Å, respectively.

Quantitative comparison of tropomyosin shifts

To make a quantitative comparison of the position of tropomyosin among the different perturbations, we calculated the root-mean-square deviations (RMSDs). First, we fitted the pruned C-state model without the troponin complexes (PDB: 6KN8) into each of the maps using the *dock_in_map* function in PHENIX[41]. The resulting models were used to calculate RMSD values in ChimeraX[42] with only the tropomyosins selected.

Visualization and figure preparation

To better visualize the subcellular arrangement of the variety of macromolecules in cardiomyocytes (Fig. 2), the macromolecules were semi-automatically annotated using the convolutional neural network algorithm in EMAN2[43]. The segmented surfaces were then visualized in UCSF ChimeraX. Tomographic slices used to visualize the myofibrils were prepared in 3dmod[44]. All figures with subvolume-averaged maps were created using UCSF ChimeraX[42]. ChimeraX[42] and Napri[45] were used to visualize the tomograms and prepare movies.

Data availability

Cryo-ET density maps generated in this study will be available in the EM Data Bank with the following accession codes: EMD-XXXXX (The human thin filament), EMD-XXXXX (The human thin filament with the troponin complex), EMD-XXXXX (The human thin filament with MYH7$^{WT/G256E}$ mutation), EMD-XXXXX (The human thin filament with MYH7$^{WT/G256E}$ mutation with the troponin complex),EMD-XXXXX (The human thin filament treated with doxorubicin), and EMD-XXXXX (The human thin filament treated with doxorubicin with the troponin complex). Publicly available entries used in this study are EMD-0728/PDB (B-state), EMD-0729/PDB 6KN8 (B-state), and EMD-13996 (M-state).

References

1. Plitzko, J. & Baumeister, W. P. in *Springer Handbook of Microscopy* (eds. Hawkes, P. W. & Spence, J. C. H.) 2–2 (Springer International Publishing, 2019). doi:10.1007/978-3-030-00069-1_4
2. Dai, W., Fu, C., Raytcheva, D., Flanagan, J., Khant, H. A., Liu, X., Rochat, R. H., Haase-Pettingell, C., Piret, J., Ludtke, S. J., Nagayama, K., Schmid, M. F., King, J. A. & Chiu, W. Visualizing virus assembly intermediates inside marine cyanobacteria. *Nature* **502,** 707–710 (2013).
3. Mahamid, J., Pfeffer, S., Schaffer, M., Villa, E., Danev, R., Cuellar, L. K., Förster, F., Hyman, A. A., Plitzko, J. M. & Baumeister, W. Visualizing the molecular sociology at the HeLa cell nuclear periphery. *Science* **351,** 969–972 (2016).
4. Wu, G.-H., Mitchell, P. G., Galaz-Montoya, J. G., Hecksel, C. W., Sontag, E. M., Gangadharan, V., Marshman, J., Mankus, D., Bisher, M. E., Lytton-Jean, A. K. R., Frydman, J., Czymmek, K. & Chiu, W. Multi-scale 3D Cryo-Correlative Microscopy for Vitrified Cells. *Structure* **28,** 1231-1237.e3 (2020).
5. Schiøtz, O. H., Kaiser, C. J. O., Klumpe, S., Morado, D. R., Poege, M., Schneider, J., Beck, F., Thompson, C. & Plitzko, M. J. Serial Lift-Out – Sampling the Molecular Anatomy of Whole Organisms. 2023.04.28.538734 Preprint at https://doi.org/10.1101/2023.04.28.538734 (2023)
6. Wang, Z., Grange, M., Pospich, S., Wagner, T., Kho, A. L., Gautel, M. & Raunser, S. Structures from intact myofibrils reveal mechanism of thin filament regulation through nebulin. *Science* **375,** eabn1934

7. Tamborrini, D., Wang, Z., Wagner, T., Tacke, S., Stabrin, M., Grange, M., Kho, A. L., Rees, M., Bennett, P., Gautel, M. & Raunser, S. In situ structures from relaxed cardiac myofibrils reveal the organization of the muscle thick filament. 2023.04.11.536387 Preprint at https://doi.org/10.1101/2023.04.11.536387 (2023)
8. Burbaum, L., Schneider, J., Scholze, S., Böttcher, R. T., Baumeister, W., Schwille, P., Plitzko, J. M. & Jasnin, M. Molecular-scale visualization of sarcomere contraction within native cardiomyocytes. *Nat Commun* **12,** 4086 (2021).
9. Lee, S., Roest, A. S. V., Blair, C. A., Kao, K., Bremner, S. B., Childers, M. C., Pathak, D., Heinrich, P., Lee, D., Chirikian, O., Mohran, S., Roberts, B., Smith, J. E., Jahng, J. W., Paik, D. T., Wu, J. C., Gunawardane, R. N., Spudich, J. A., Ruppel, K., Mack, D., Pruitt, B. L., Regnier, M., Wu, S. M. & Bernstein, D. Multi-scale models reveal hypertrophic cardiomyopathy MYH7 G256E mutation drives hypercontractility and elevated mitochondrial respiration. 2023.06.08.544276 Preprint at https://doi.org/10.1101/2023.06.08.544276 (2023)
10. Burridge, P. W., Li, Y. F., Matsa, E., Wu, H., Ong, S.-G., Sharma, A., Holmström, A., Chang, A. C., Coronado, M. J., Ebert, A. D., Knowles, J. W., Telli, M. L., Witteles, R. M., Blau, H. M., Bernstein, D., Altman, R. B. & Wu, J. C. Human induced pluripotent stem cell–derived cardiomyocytes recapitulate the predilection of breast cancer patients to doxorubicin-induced cardiotoxicity. *Nature Medicine* **22,** 547–556 (2016).
11. Ribeiro, A. J. S., Ang, Y.-S., Fu, J.-D., Rivas, R. N., Mohamed, T. M. A., Higgs, G. C., Srivastava, D. & Pruitt, B. L. Contractility of single cardiomyocytes differentiated from pluripotent stem cells depends on physiological shape and substrate stiffness. *PNAS* **112,** 12705–12710 (2015).
12. Powers, J. D., Malingen, S. A., Regnier, M. & Daniel, T. L. The Sliding Filament Theory Since Andrew Huxley: Multiscale and Multidisciplinary Muscle Research. *Annu. Rev. Biophys.* **50,** 373–400 (2021).
13. Spudich, J. A. The myosin swinging cross-bridge model. *Nat Rev Mol Cell Biol* **2,** 387–392 (2001).
14. McKillop, D. F. & Geeves, M. A. Regulation of the interaction between actin and myosin subfragment 1: evidence for three states of the thin filament. *Biophysical Journal* **65,** 693–701 (1993).
15. Lim, C. C., Zuppinger, C., Guo, X., Kuster, G. M., Helmes, M., Eppenberger, H. M., Suter, T. M., Liao, R. & Sawyer, D. B. Anthracyclines Induce Calpain-dependent Titin Proteolysis and Necrosis in Cardiomyocytes*. *Journal of Biological Chemistry* **279,** 8290–8299 (2004).

16. Tobacman, L. S. Troponin Revealed: Uncovering the Structure of the Thin Filament On-Off Switch in Striated Muscle. *Biophys J* **120,** 1–9 (2021).

17. Yamada, Y., Namba, K. & Fujii, T. Cardiac muscle thin filament structures reveal calcium regulatory mechanism. *Nature Communications* **11,** 153 (2020).

18. Risi, C. M., Pepper, I., Belknap, B., Landim-Vieira, M., White, H. D., Dryden, K., Pinto, J. R., Chase, P. B. & Galkin, V. E. The structure of the native cardiac thin filament at systolic Ca2+ levels. *Proceedings of the National Academy of Sciences* **118,** e2024288118 (2021).

19. Schneider, C. A., Rasband, W. S. & Eliceiri, K. W. NIH Image to ImageJ: 25 years of image analysis. *Nat Methods* **9,** 671–675 (2012).

20. Engel, L., Gaietta, G., Dow, L. P., Swif, M. F., Pardon, G., Volkmann, N., Weis, W. I., Hanein, D. & Pruitt, B. L. Extracellular matrix micropatterning technology for whole cell cryogenic electron microscopy studies. *J. Micromech. Microeng.* **29,** 115018 (2019).

21. Engel, L., rgsheld, Vasquez, C. G., Weis, W. I. & Dunn, A. R. Micropatterning EM grids for cryo-electron tomography of cells. *protocols.io* (2022). at <https://www.protocols.io/view/micropatterning-em-grids-for-cryo-electron-tomogra-bz22p8ge>

22. Engel, L., Vasquez, C. G., Montabana, E. A., Sow, B. M., Walkiewicz, M. P., Weis, W. I. & Dunn, A. R. Lattice micropatterning for cryo-electron tomography studies of cell-cell contacts. *Journal of Structural Biology* **213,** 107791 (2021).

23. Kreitzer, F. R., Salomonis, N., Sheehan, A., Huang, M., Park, J. S., Spindler, M. J., Lizarraga, P., Weiss, W. A., So, P.-L. & Conklin, B. R. A robust method to derive functional neural crest cells from human pluripotent stem cells. *Am J Stem Cells* **2,** 119–131 (2013).

24. Roberts, B., Haupt, A., Tucker, A., Grancharova, T., Arakaki, J., Fuqua, M. A., Nelson, A., Hookway, C., Ludmann, S. A., Mueller, I. A., Yang, R., Horwitz, R., Rafelski, S. M. & Gunawardane, R. N. Systematic gene tagging using CRISPR/Cas9 in human stem cells to illuminate cell organization. *Mol Biol Cell* **28,** 2854–2874 (2017).

25. Roberts, B., Hendershott, M. C., Arakaki, J., Gerbin, K. A., Malik, H., Nelson, A., Gehring, J., Hookway, C., Ludmann, S. A., Yang, R., Haupt, A., Grancharova, T., Valencia, V., Fuqua, M. A., Tucker, A., Rafelski, S.

M. & Gunawardane, R. N. Fluorescent Gene Tagging of Transcriptionally Silent Genes in hiPSCs. *Stem Cell Reports* **12,** 1145–1158 (2019).

26. Lian, X., Bao, X., Zilberter, M., Westman, M., Fisahn, A., Hsiao, C., Hazeltine, L. B., Dunn, K. K., Kamp, T. J. & Palecek, S. P. Chemically defined, albumin-free human cardiomyocyte generation. *Nat Methods* **12,** 595–596 (2015).
27. Lee, J., Termglinchan, V., Diecke, S., Itzhaki, I., Lam, C. K., Garg, P., Lau, E., Greenhaw, M., Seeger, T., Wu, H., Zhang, J. Z., Chen, X., Gil, I. P., Ameen, M., Sallam, K., Rhee, J.-W., Churko, J. M., Chaudhary, R., Chour, T., Wang, P. J., Snyder, M. P., Chang, H. Y., Karakikes, I. & Wu, J. C. Activation of PDGF pathway links LMNA mutation to dilated cardiomyopathy. *Nature* **572,** 335–340 (2019).
28. Nishiga, M., Qi, L. S. & Wu, J. C. in *Pluripotent Stem-Cell Derived Cardiomyocytes* (ed. Yoshida, Y.) 261–281 (Springer US, 2021). doi:10.1007/978-1-0716-1484-6_23
29. Schaffer, M., Engel, B. D., Laugks, T., Mahamid, J., Plitzko, J. M. & Baumeister, W. Cryo-focused Ion Beam Sample Preparation for Imaging Vitreous Cells by Cryo-electron Tomography. *Bio Protoc* **5,** (2015).
30. Wagner, F. R., Watanabe, R., Schampers, R., Singh, D., Persoon, H., Schaffer, M., Fruhstorfer, P., Plitzko, J. & Villa, E. Preparing samples from whole cells using focused-ion-beam milling for cryo-electron tomography. *Nature Protocols* 1–30 (2020). doi:10.1038/s41596-020-0320-x
31. Wolff, G., Limpens, R. W. A. L., Zheng, S., Snijder, E. J., Agard, D. A., Koster, A. J. & Bárcena, M. Mind the gap: Micro-expansion joints drastically decrease the bending of FIB-milled cryo-lamellae. *Journal of Structural Biology* **208,** 107389 (2019).
32. Mastronarde, D. N. Automated electron microscope tomography using robust prediction of specimen movements. *Journal of Structural Biology* **152,** 36–51 (2005).
33. Hagen, W. J. H., Wan, W. & Briggs, J. A. G. Implementation of a cryo-electron tomography tilt-scheme optimized for high resolution subtomogram averaging. *Journal of Structural Biology* **197,** 191–198 (2017).
34. Zheng, S. Q., Palovcak, E., Armache, J.-P., Verba, K. A., Cheng, Y. & Agard, D. A. MotionCor2: anisotropic correction of beam-induced motion for improved cryo-electron microscopy. *Nature Methods* **14,** 331–332 (2017).
35. Zheng, S., Wolff, G., Greenan, G., Chen, Z., Faas, F. G. A., Bárcena, M., Koster, A. J., Cheng, Y. & Agard,

D. A. AreTomo: An integrated software package for automated marker-free, motion-corrected cryo-electron tomographic alignment and reconstruction. *Journal of Structural Biology: X* **6,** 100068 (2022).

36. Liu, Y.-T., Zhang, H., Wang, H., Tao, C.-L., Bi, G.-Q. & Zhou, Z. H. Isotropic Reconstruction of Electron Tomograms with Deep Learning. *bioRxiv* 2021.07.17.452128 (2021). doi:10.1101/2021.07.17.452128
37. Tegunov, D. & Cramer, P. Real-time cryo-electron microscopy data preprocessing with Warp. *Nat Methods* 1–7 (2019). doi:10.1038/s41592-019-0580-y
38. Moebel, E., Martinez-Sanchez, A., Lamm, L., Righetto, R. D., Wietrzynski, W., Albert, S., Larivière, D., Fourmentin, E., Pfeffer, S., Ortiz, J., Baumeister, W., Peng, T., Engel, B. D. & Kervrann, C. Deep learning improves macromolecule identification in 3D cellular cryo-electron tomograms. *Nat Methods* **18,** 1386–1394 (2021).
39. Zivanov, J., Otón, J., Ke, Z., Qu, K., Morado, D., Castaño-Díez, D., Kügelgen, A. von, Bharat, T. A. M., Briggs, J. A. G. & Scheres, S. H. W. A Bayesian approach to single-particle electron cryo-tomography in RELION-4.0. 2022.02.28.482229 Preprint at https://doi.org/10.1101/2022.02.28.482229 (2022)
40. Tegunov, D., Xue, L., Dienemann, C., Cramer, P. & Mahamid, J. Multi-particle cryo-EM refinement with M visualizes ribosome-antibiotic complex at 3.5 Å in cells. *Nature Methods* **18,** 186–193 (2021).
41. Liebschner, D., Afonine, P. V., Baker, M. L., Bunkóczi, G., Chen, V. B., Croll, T. I., Hintze, B., Hung, L.-W., Jain, S., McCoy, A. J., Moriarty, N. W., Oeffner, R. D., Poon, B. K., Prisant, M. G., Read, R. J., Richardson, J. S., Richardson, D. C., Sammito, M. D., Sobolev, O. V., Stockwell, D. H., Terwilliger, T. C., Urzhumtsev, A. G., Videau, L. L., Williams, C. J. & Adams, P. D. Macromolecular structure determination using X-rays, neutrons and electrons: recent developments in Phenix. *Acta Cryst D* **75,** 861–877 (2019).
42. Goddard, T. D., Huang, C. C., Meng, E. C., Pettersen, E. F., Couch, G. S., Morris, J. H. & Ferrin, T. E. UCSF ChimeraX: Meeting modern challenges in visualization and analysis. *Protein Sci.* **27,** 14–25 (2018).
43. Chen, M., Dai, W., Sun, S. Y., Jonasch, D., He, C. Y., Schmid, M. F., Chiu, W. & Ludtke, S. J. Convolutional neural networks for automated annotation of cellular cryo-electron tomograms. *Nature Methods* **14,** 983–985 (2017).
44. Kremer, J. R., Mastronarde, D. N. & McIntosh, J. R. Computer Visualization of Three-Dimensional Image Data Using IMOD. *Journal of Structural Biology* **116,** 71–76 (1996).

45. Ahlers, J., Althviz Moré, D., Amsalem, O., Anderson, A., Bokota, G., Boone, P., Bragantini, J., Buckley, G., Burt, A., Bussonnier, M., Can Solak, A., Caporal, C., Doncila Pop, D., Evans, K., Freeman, J., Gaifas, L., Gohlke, C., Gunalan, K., Har-Gil, H., Harfouche, M., Harrington, K. I. S., Hilsenstein, V., Hutchings, K., Lambert, T., Lauer, J., Lichtner, G., Liu, Z., Liu, L., Lowe, A., Marconato, L., Martin, S., McGovern, A., Migas, L., Miller, N., Muñoz, H., Müller, J.-H., Nauroth-Kreß, C., Nunez-Iglesias, J., Pape, C., Pevey, K., Peña-Castellanos, G., Pierré, A., Rodríguez-Guerra, J., Ross, D., Royer, L., Russell, C. T., Selzer, G., Smith, P., Sobolewski, P., Sofiiuk, K., Sofroniew, N., Stansby, D., Sweet, A., Vierdag, W.-M., Wadhwa, P., Weber Mendonça, M., Windhager, J., Winston, P. & Yamauchi, K. napari: a multi-dimensional image viewer for Python. (2023). doi:10.5281/zenodo.8115575

Acknowledgements

We thank Gong-her Wu, Patrick Mitchell, and Grigore Pintilie and members of the Chiu and Wu lab for helpful discussions. This research was supported by: T32 NIBIB 2T32EB009035 and NHLBI K99HL161392 (to R.A.W.), and other support including NIH S10OD021600, DOE (BERFWP 100463), Silicon Valley Community Foundation Chan Zuckerberg Initiative (2021-234593) (to W.C.). Some of this work was performed at the Stanford-SLAC Cryo-EM Center and the Stanford-SLAC CryoET Specimen Preparation Center under the support of the National Institutes of Health Common Fund's Transformative High Resolution Cryo-electron Microscopy Program (U24GM139166 and U24GM129541). The authors would also like to thank the following SLAC cryoEM personnel for their invaluable support and assistance: Patrick Mitchell, Megan Mayer, Corey Hecksel, Chensong Zhang and Lydia-Marie Joubert. Some of the work was performed at nano@Stanford labs, which are supported by the National Science Foundation as part of the National Nanotechnology Coordinated Infrastructure under award ECCS-2026822. M.N. was supported by NHLBI K99HL166773.

Author contributions

R.A.W. and W.C. conceived the project and designed the experiments. W.C. and R.A.W. supervised the project and acquired funding. M.N., A.S.V., and P.G. prepared hiPSC-CM samples under the supervision of J.C.W., J.A.S., and D.B. L.E. patterned electron microscopy grids under the supervision of A.R.D. with input from R.A.W., A.S.V., and M.N. R.A.W. processed samples and acquired data. R.A.W. processed and analyzed the data with help from G.C.M., and A.C.W. in annotation and M.F.S. with initial interpretation. R.A.W. and W.C. wrote the manuscript draft with the help from all authors.

Competing interests

J.C.W. is a co-founder and on the SAB of Greenstone Biosciences, but the work was done independently. J.A.S. is a co-founder and consultant for Cytokinetics Inc. and owns stock in the company, which has a focus on therapeutic treatments for cardiomyopathies and other muscle diseases, but the work was done independently. The other authors declare no competing interests.

Additional information

Supplementary materials

Table S1. CryoET data collection and refinement statistics of vitrified and milled hiPSC-cardiomyocytes

	Thin filament from WT cells		**Thin filament from MYH7$^{WT/G256E}$ cells**		**Thin filament from doxorubicin-treated cells**	
Microscopy						
Microscope	Titan Krios 3Gi		Titan Krios 3G		Titan Krios 3Gi	
Voltage(kV)	300		300		300	
Camera	K3/BioQuantum, CDS		K3/BioQuantum		K3/BioQuantum, CDS	
Slit width(eV)	15		20		15	
Pixel size (Å)	2.13		2.20		2.13	
Defocus range (μm)	3.5-5.0		3.5-5.0		3.5-5.0	
Tilt range[a] (pre-tilt, increment)	-48°/+48° (-9°, 3°)		-60°/+60° (0°, 2°)		-60°/+60° (0°, 3°)	
Tilt scheme	Dose-symmetric		Dose-symmetric		Dose-symmetric	
Total dose (e^-/Å^2)	~105		~120		~115	
Number of cells/lamellae	3		3		3	
Number of tomograms	12		8		14	
3D refinement statistics	**Without the troponin complex**	**With the troponin complex**	**Without the troponin complex**	**With the troponin complex**	**Without the troponin complex**	**With the troponin complex**
Number of sub-volumes	16,451	1,463	15,147	2,114	7,555	2,737
Symmetry	C1	C1	C1	C1	C1	C1
Resolution (Å)	8.7	19.5	9.3	12.4	9.5	12.4

[a] Tilt angle range used only for data collection relative to the pre-tilt.

Supplementary figures

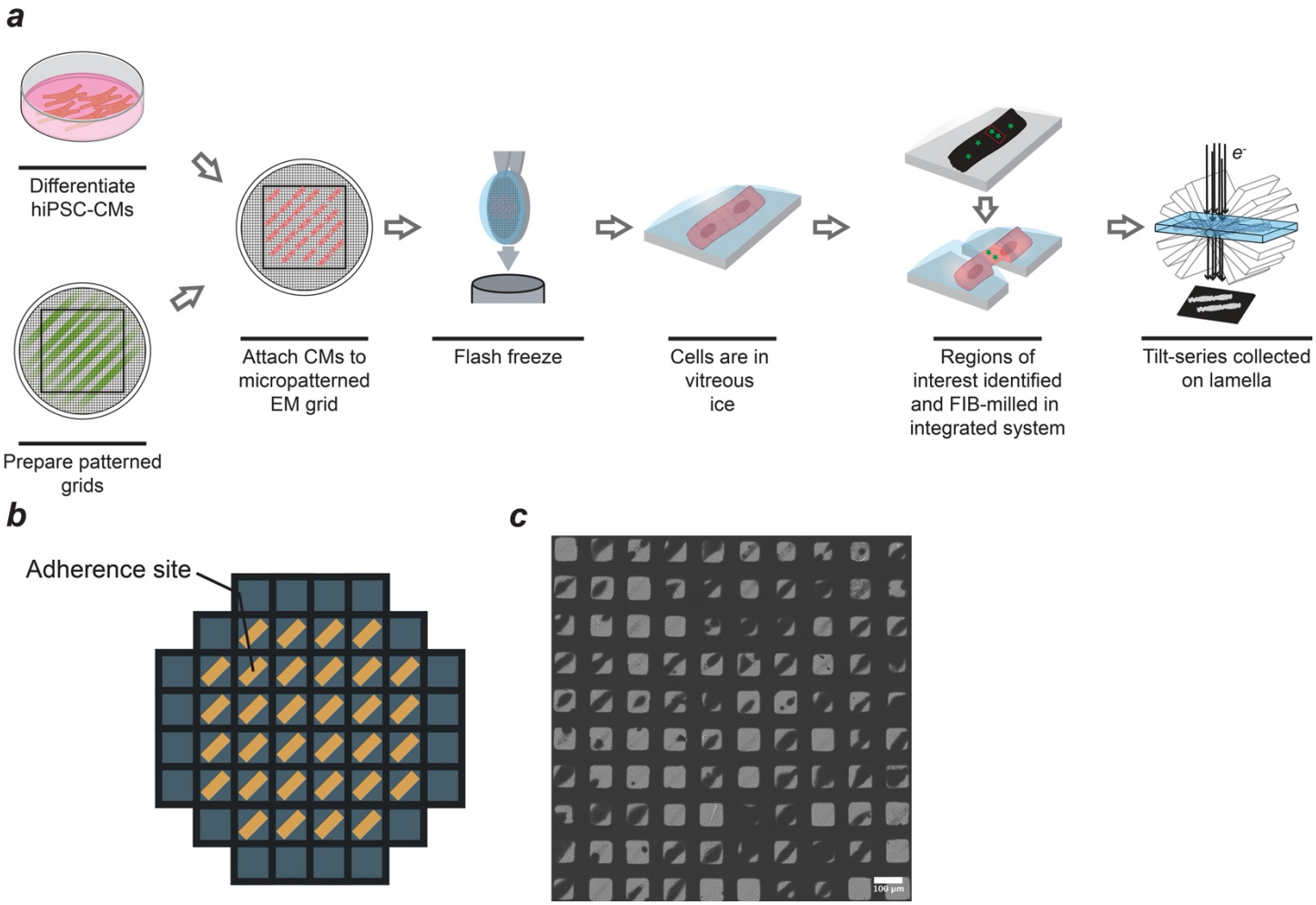

Fig. S1 | A complete experimental workflow for visualizing cardiomyocytes using cryoET

a Human induced-pluripotent stem cells (hiPSCs) are differentiated into cardiomyocytes (hiPSC-CMs) then attached to micropatterned EM grids. Once attached to the grid, cells are flash frozen to encase in vitreous ice. All subsequent steps are performed at cryogenic temperatures. Regions of interest within the cells are identified using correlated light and electronic microscopy then milled using a focused ion beam to create thin lamellae. Finally, a tilt-series is collected in the transmission electron microscope for subsequent reconstruction as a 3-dimensional tomogram.

b The diagonal rectangle pattern (ratio 1:7) used to guide hiPSC-CM adherence and shape.

c Cryo-TEM atlas showing cells attached to a micropatterned EM grid.

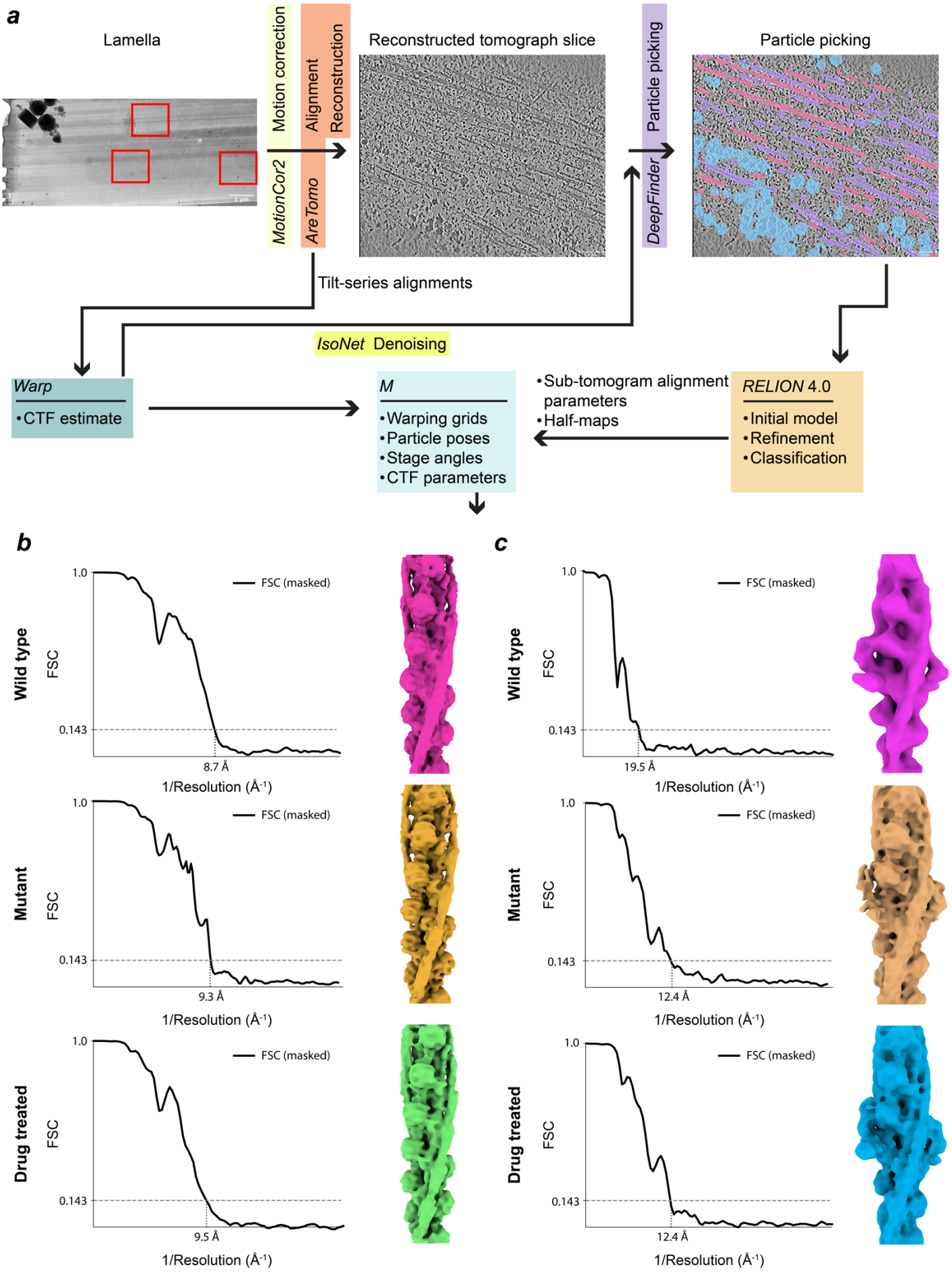
a
Lamella
Motion correction
MotionCor2
Alignment
Reconstruction
AreTomo
Reconstructed tomograph slice
Particle picking
DeepFinder
Particle picking
Tilt-series alignments
IsoNet Denoising
Warp
•CTF estimate
M
•Warping grids
•Particle poses
•Stage angles
•CTF parameters
•Sub-tomogram alignment parameters
•Half-maps
RELION 4.0
•Initial model
•Refinement
•Classification
b
c
Wild type
Mutant
Drug treated
FSC
FSC (masked)
1.0
0.143
8.7 Å
9.3 Å
9.5 Å
19.5 Å
12.4 Å
12.4 Å
1/Resolution (Å-1)

Fig. S2 | The data processing workflow

a A schematic of the data processing workflow, as detailed in the **Methods**. Tilt series were collected on regions of interest (red boxes within the lamella), MotionCor2 was used for motion correction, and AreTomo was used for alignment and reconstruction of the 3D tomogram. Alignments from AreTomo were passed to Warp to generate a CTF estimate and the CTF Estimate was passed to IsoNet to denoise the tomogram. Particle picking was performed in denoised tomograms using DeepFinder, and particle coordinates were passed to RELION 4.0. In RELION, an initial model was generated then refined, followed by particle classification. Sub-tomogram alignment parameters and half-maps were then passed to M for further refinement.

b Fourier shell correlation (FSC) plots are shown for the thin filaments reconstructed from wild-type (top) mutant ($MYH7^{WT/G256E}$, middle) and drug-treated (doxorubicin, bottom) cells. Estimates of model resolution are derived from these plots for the masked data. The corresponding models are shown to the right.

c Fourier shell correlation (FSC) plots are shown for the thin filaments, with troponin included, reconstructed from wild-type (top) mutant ($MYH7^{WT/G256E}$, middle) and drug-treated (doxorubicin, bottom) cells. Estimates of model resolution are derived from these plots for the mask ed data. The corresponding models are shown to the right.

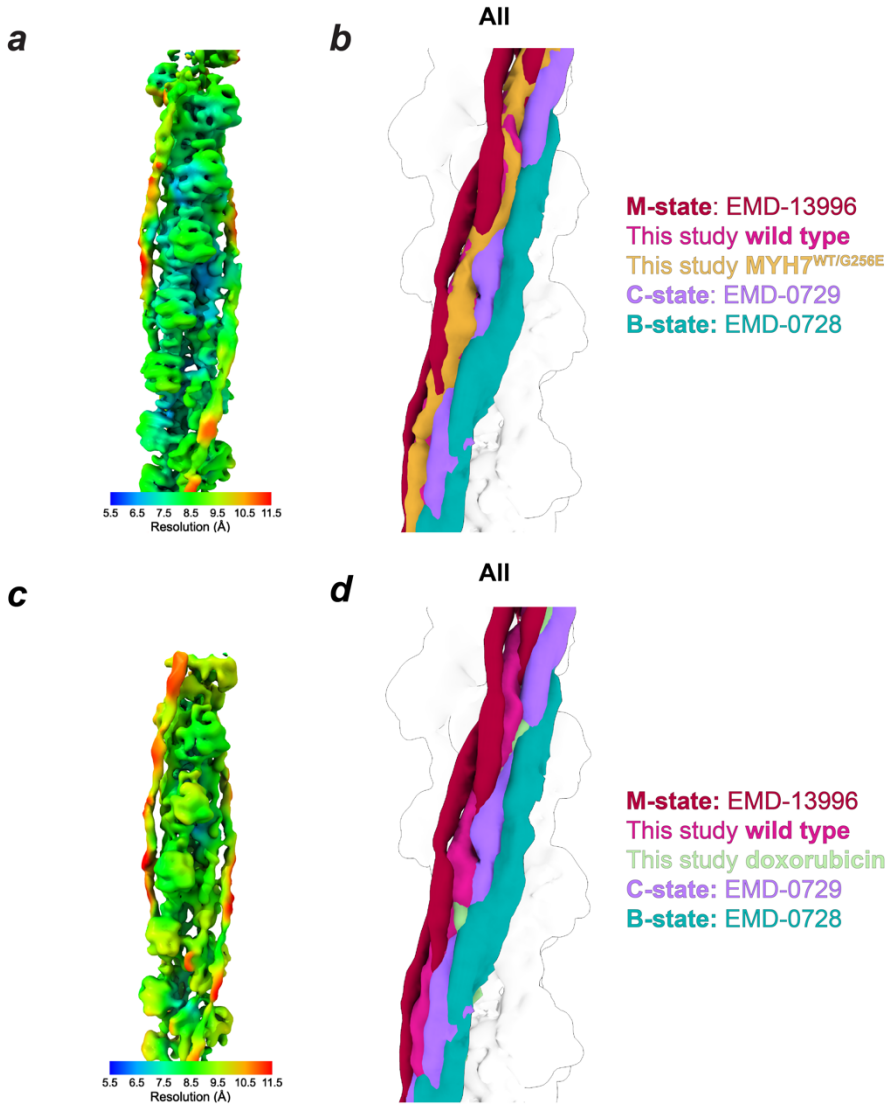

Fig. S3 | *In situ* structures of mutant and drug-treated thin filaments

a An *in situ* structure of the thin filament reconstructed from hiPSC-CMs carrying the MYH7$^{WT/G256E}$ mutation. The resolution of the reconstruction is shown as a colormap.

b The position of tropomyosin in the MYH7$^{WT/G256E}$ background compared to wild type (hot pink), the M-state (burgundy), the C-state (purple) and the B-state (teal).

c An *in situ* structure of the thin filament reconstructed from wild type hiPSC-CMs treated with doxorubicin (100 nM). The resolution of the reconstruction is shown as a colormap.

d The position of tropomyosin in doxorubicin-treated cells compared to wild type (hot pink), the M-state (burgundy), the C-state (purple) and the B-state (teal).

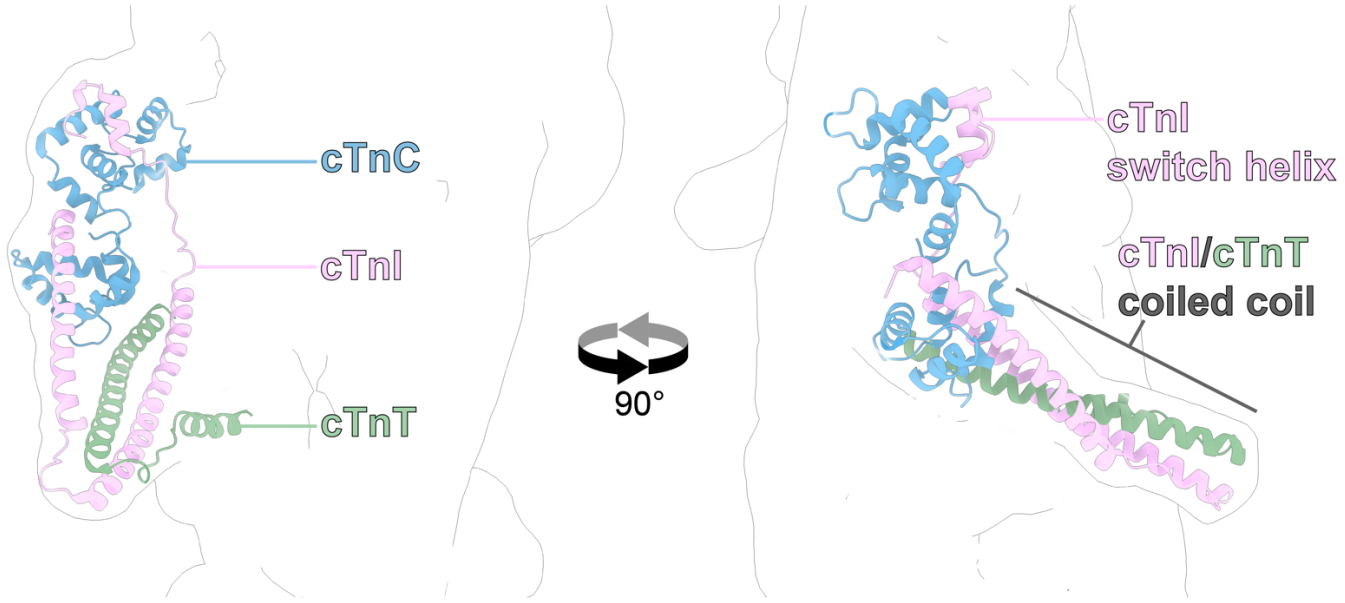

Fig. S4 | Features of the troponin complex

A labeled model (PDB: 6KN8) of the troponin complex is shown in the context of the thin filament (EMD: 0729) at two angles. (*Left*) Individual subunits of the troponin complex are show as color-coded cartoons, including cTnC (blue), cTnI (pink), and cTnT (green). (*Right*) Features of the complex mentioned in the text are shown, including the cTnI switch helix and the cTnI-cTnT coiled-coil.

Movies

Movie S1. Visualization of an annotated tomogram with myofibrils. The video shows a series of slices along the Z-axis of a tomogram to reveal details of the myofibril and its cellular context. The original view shows ribosomes, glycogen, and vesicles surrounding myofibrils. In the next section of the video, the image is zoomed in to reveal the thin filament, the thick filament, and myosin heads protruding from the thick filament. Next, results from annotating particles using *DeepFinder* are shown as a color-coding. Annotated particles include the thin filament (purple), thick filament (pink), and ribosomes (blue). A scale bar is shown in the bottom right corner of the video.

Movie S2. Segmentation of a tomogram from cardiomyocytes reveals the arrangement of a variety of macromolecules. A series of slices are shown through a tomogram which progressively reveal particles that were segmented in the analysis. Particles are color-coded according to classification, including the thin filament (purple), thick filament (pink), glycogen (yellow), ribosomes (blue), and vesicles (green).

Movie S3. Structural diversity of the human thin filament highlighting the lower troponin complex under different conditions. A map of the thin filament with the troponin complex determined *in vitro* (EMD:0729) is morphed into maps from this study reconstructed from wild type (pink), $MYH7^{WT/G256E}$ (gold), and doxorubicin-treated (blue) hiPSC-CMs. Both the upper (top right) and lower (bottom left) troponin complexes are shown. The map is oriented to focus on conformational changes in the lower troponin complex.

Movie S4: Structural diversity of the human thin filament highlighting the upper troponin complex under different conditions. The same set of maps are shown as in **Movie S3**, but maps are rotated to focus on conformational changes in the upper troponin complex.

Digital Files

Digital Files S1: A digital pattern file of rectangles with a 1:7 aspect ratio and areas of 1500 μm^2 (14.64 µm by 102.465 µm), specifically designed for micropatterning electron microscopy grids for cardiomyocytes.

Digital Files S2: A digital pattern file of rectangles with a 1:7 aspect ratio and areas of 2000 μm^2 (16.903 µm by 118.32 µm), specifically designed for micropatterning electron microscopy grids for cardiomyocytes.